Biosensors and Bioelectronics 287 (2025) 117743

Contents lists available at ScienceDirect

Biosensors and Bioelectronics

journal homepage: www.elsevier.com/locate/bios

Ultrasensitive detection of miRNA with single-nucleotide resolution using a high-electron-mobility transistor biosensor combined with splint-ligation

Chenyang Yang [a,f,1], Jingya Tang [a,f,1], Jianwen Sun [b,1], Zewen Liu [b], Guoqi Zhang [d], Zhe Li [e], Dian-Bing Wang [a,*], Xian-En Zhang [a,c,f,**]

[a] State Key Laboratory of Biomacromolecules, Institute of Biophysics, Chinese Academy of Sciences, Beijing, 100101, China
[b] School of Integrated Circuits, Tsinghua University, Beijing, 10084, China
[c] Faculty of Synthetic Biology, Shenzhen University of Advanced Technology, Shenzhen, 518055, China
[d] Department of Microelectronics, Delft University of Technology, 2628 CD, Delft, the Netherlands
[e] Precision Scientific (Beijing) Co. Ltd., Beijing, 100085, China
[f] University of Chinese Academy of Science, Beijing, 100049, China

ARTICLE INFO

Keywords:
Biosensors
Splint-ligation
miRNA detection
AlGaN/GaN HEMT
Specificity

ABSTRACT

The use of microRNAs as clinical cancer biomarkers is hindered by the absence of accurate, sensitive and rapid assays for their detection in biofluids. Here we report a biosensing approach, SpLig-HEMT, that combines an RNA splint-ligation reaction with an AlGaN/GaN high-electron-mobility transistor biosensor for ultrasensitive miRNA detection. In this system, HEMT functions as a highly effective voltage amplifier to enhance detection sensitivity, while the splint-ligation reaction ensures precise discrimination of single-nucleotide mutations. By detecting miRNA-21, the SpLig-HEMT biosensor achieves an exceptional limit of detection of 10^{-18} M within 30 min, with a dynamic range from 10^{-18} M to 10^{-13} M. No detectable response is observed for one-mismatch miR-21. Furthermore, the SpLig-HEMT biosensor enables direct analysis of blood serum samples, effectively distinguishing between healthy individuals and patients with ovarian cancer. This study addresses critical challenges in miRNA detection and presents a promising tool for cancer diagnosis and prognosis.

1. Introduction

MicroRNAs (miRNAs) are short, noncoding single-stranded RNA molecules, typically 18–23 nucleotides in length, that regulate gene expression by binding to the 3' untranslated region of target mRNAs (Navickas et al., 2016). Although initially found in tissues, miRNAs have since been discovered in various body fluids, including serum and urine. Extensive studies have demonstrated that miRNAs can regulate oncogenes and tumor suppressor genes, thereby contributing to tumorigenesis (Matsuzaki and Ochiya, 2017; Wang et al., 2014). This highlights the potential of circulating miRNAs as key biomarkers for early detection of cancer. For example, miRNA-21 is frequently overexpressed in the serum of patients with various malignancies and plays a crucial role in processes that promote tumorigenesis and metastasis. However, the transition of miRNA-based diagnostics from proof-of-concept studies to clinical practice remains incomplete. A significant proportion of miRNAs are encapsulated within exosomes or bound to protein complexes, leaving only trace amounts of freely circulating miRNAs in serum (Li et al., 2021). Because free-circulating miRNAs are typically present at femtomolar concentrations, which are even lower in early-stage patients (Yokoi et al., 2018), the development of ultrasensitive detection techniques is required. Moreover, genetic variations in miRNA genes can influence miRNA-mediated regulatory functions, further disrupting regulatory networks. Several studies have found that single-nucleotide polymorphisms (SNPs) can contribute to phenotypic variations and, in some cases, promote cancer metastasis (Gong et al., 2012; Hughes et al., 2011; Richardson et al., 2013). Therefore, miRNA detection methods must provide single-nucleotide resolution, combined with enhanced sensitivity, specificity, and versatility, to facilitate wide clinical applications.

Various methods have been developed for miRNA detection, and reverse transcription quantitative polymerase chain reaction (RT-PCR)

* Corresponding author.
** Corresponding author. State Key Laboratory of Biomacromolecules, Institute of Biophysics, Chinese Academy of Sciences, Beijing 100101, China.
E-mail addresses: wangdb@moon.ibp.ac.cn (D.-B. Wang), zhangxe@ibp.ac.cn (X.-E. Zhang).
[1] These authors contributed equally.

https://doi.org/10.1016/j.bios.2025.117743
Received 20 March 2025; Received in revised form 27 May 2025; Accepted 30 June 2025
Available online 2 July 2025

is currently considered the gold standard (Chen et al., 2005). Because of the short length of miRNAs, the addition of a poly(A) tail is typically required to facilitate reverse transcription and subsequent PCR amplification (Klasens et al., 1998). As an alternative to thermal-cycling-based qPCR, several isothermal detection methods have been developed to improve miRNA assays, including rolling-circle amplification (Wang et al., 2020), loop-mediated isothermal amplification (Li et al., 2011), and hybridization chain reaction (Choi et al., 2010). Although these methods simplify workflows and enhance operational convenience, they have limitations in terms of sensitivity, specificity, and the ability to differentiate sequence mutations (Nabhan et al., 2015). Clustered regularly interspaced short palindromic repeat (CRISPR) technologies have emerged as promising tools for nucleic acid detection, offering single-nucleotide resolution (Chen et al., 2023). Nevertheless, current CRISPR-based methods are constrained by their dependence on the protospacer adjacent motif (PAM), which limits their ability to detect single-nucleotide mutations that occur distal to the PAM site (Balderston et al., 2021).

Several biosensors, including optical (Zheng et al., 2022) and electrochemical sensors (Bruch et al., 2019), have been developed for miRNA detection. Field-effect transistors (FETs) are electrical sensors that have gained widespread use in biomarker assays owing to their real-time measurements and label-free detection. Among various FET sensors, AlGaN/GaN high-electron-mobility transistor sensors are particularly known for their exceptional sensitivity and biocompatibility. As shown in Fig. S1, the HEMT channel is confined within a narrow quantum well and operates as a two-dimensional channel rather than a three-dimensional channel. This unique configuration enables efficient on-site amplification of the input signal and low-noise recording (Sarangadharan et al., 2018; Varghese et al., 2018). When used for protein detection, the HEMT biosensor achieves detection limits within the attomolar (aM) range (Yang et al., 2024). However, the sensitivity of these sensors for detecting miRNAs is lower than that for detecting proteins and other biomolecules. This is likely because of the relatively low charge carried by the miRNAs, which may limit their interaction with the sensing area and reduce the overall sensitivity.

Here we report SpLig-HEMT, an integrated system combining splint-ligation with HEMT sensor for the miRNA detection. The splint-ligation reaction facilitates the precise joining of two nucleic acid strands using a complementary "splint" DNA or RNA molecule. While the current methods, such as synthetic biology-assisted diagnostics (INSPECTR (Phillips et al., 2023)) and aptamer-based detection (SENSR(Woo et al., 2020)), have demonstrated the utility of splint-ligated DNA probes for RNA detection, these approaches rely on nucleic acid amplification or synthesis and lack sufficient characterization of single-nucleotide discrimination capabilities. In this work, SpLig-HEMT addresses these constraints through two mechanisms: First, the direct transduction of ligation-induced electrical signal alteration eliminates target amplification requirements, enabling single-molecule detection. Second, a dual-recognition architecture, which combines sequence-specific DNA probes with miRNA-responsive ligase activity, can achieve single-nucleotide resolution. To validate the performance of SpLig-HEMT, we implement our workflow in the context of detecting cancer-related miRNA and clinical samples, and both excellent sensitivity and specificity have been achieved within 30 min.

2. Materials and methods

2.1. Materials

The synthetic DNA probe and miRNA were purified using high-performance liquid chromatography and (Sangon Biotech Co., Ltd., China). The ssDNA and miRNA solution were stored at −20 °C. The base pairs of all nucleotide sequences are listed in Table S1. Tris (2-carboxyethyl) phosphine hydrochloride (TCEP: 10 mM) and DEPC water (DNase, RNase-free) were also obtained from Sangon Biotech Co., Ltd. The SplintR ligase was obtained from New England Biolabs.

AlGaN/GaN heterostructure epilayers were grown on a <111> silicon wafer with a diameter of 100 mm and thickness of 675 μm using metal-organic chemical vapor deposition. The epitaxial structure consisted of an undoped GaN buffer layer (500 nm), an AlN interlayer (0.8 nm), an undoped Al0.25Ga0.75 N barrier layer (24 nm), and a 2.5 nm GaN cap layer.

2.2. Fabrication of AlGaN/GaN HEMT

The AlGaN/GaN HEMT device was fabricated using the method described in our previous study (Yang et al., 2024). We commenced this with a mesa etching step to define the active area of the device. Subsequently, we deposited Ti/Al/Ti/Au (20/110/40/50 nm) metal contacts through evaporation, followed by a rapid thermal annealing at 870 °C for 45 s in an ambient N_2 environment. We then deposited a 200 nm plasma-enhanced chemical vapor deposition (PECVD) SiO_2 layer to isolate the device from the interconnect layer. To form metal interconnects, a Ti/Au/Ti (10/300/10 nm) layer stack was evaporated. The topside of the wafer was then passivated with a 100/200 nm PECVD SiO_2/Si_3N_4 layer. The SiO_2/Si_3N_4 layer was selectively etched using inductively coupled plasma, followed by treatment with a buffered oxide etchant to expose the contact pads and gate windows. Subsequently, a Ti/Au (2/10 nm) layer was evaporated and patterned onto the 600 μm × 600 μm gate area. A 6-μm-thick Bis-BenzoCycloButene layer was then encapsulated on the wafer and patterned using photolithography. Finally, the wafer was diced into individual devices and packaged onto printed circuit boards for integration and further testing.

2.3. RNA-splinted single-stranded DNA ligation assay

Ligation was performed according to the manufacturer's instructions. In brief, a 0.2 μl anchor probe (10 μM), 0.22 μl reporter probe (10 μM), 0.22 μl target RNA, 1 μl reaction buffer (100 mM Tris-HCl [pH: 7.4] and 500 mM KCl), and 0.5 μl SplintR ligase (25 U μl^{-1}) were added to 6.86 μl RNase-free water. In the SpLig-HEMT measurement, the anchor probe was immobilized on the Au electrode, and the component in the mixture was adjusted to RNase-free water. Next, the mixture was incubated at room temperature for 10–40 min.

2.4. Biofunctionalization of Au gate electrode

To minimize the influence of impurities, we treated the Au electrode with piranha solution (H_2O_2:H_2SO_4 = 3:7) for 1 min, washed it several times with deionized water, and dried it using N_2. The cleaned Au electrode was then immersed in TECP treated-thiol anchor probe (10 μM, 10 μL) for 6 h at room temperature. Next, the gates were treated with MCH (0.1 mM, in de-ionized water) for 30 min to block the unbinding sites on the gate surface. BSA solution (0.1 mg/mL) was further added for 30 min to block the remaining non-specific binding sites on the Au electrode.

2.5. Agarose gel electrophoresis

Gel electrophoresis was performed using a 3 % agarose gel in TBE buffer at 110 V for 30 min. Images were captured using an imager (GE, Amersham Imager 600, UK). By running samples of the ligation reaction mixture on a gel, we can visualize the presence and relative amounts of the starting material (the FAM-labeled reporter probe) and the ligation product (the newly formed, larger fragment). The intensity of the fluorescence from the FAM dye in each band is proportional to the quantity of that specific DNA fragment. We apply this principle to optimize the SplintR ligation reaction by performing the reaction under various conditions.

2.6. Device measurements

The transfer characteristic curves of the devices were plotted using a semiconductor digital source meter (2614 B; Keithley Instruments, OH, USA). After the sample addition, the gate electrode was rinsed thoroughly in deionized water and tested in water. Transfer characteristic curves were obtained with $V_G = -2$ to 1 V and $V_{DS} = 0.5$ V, and the potential shift of the gate electrode was calculated after the splint-ligation reaction. AFM (Dimension FastscanBio, Bruker) was used to measure the surface topography of Au before and after functionalization. The binding components were analyzed using XPS (ESCALAB 250Xi, Thermo Fisher).

2.7. Electrostatic potential simulations

The structure of miR-21 and miR-21-reporter probe complex were prepared using AlphaFold (Jumper et al., 2021) using the gene sequence of miR-21 and reporter probe. The APBS software was used to solve the non-linear Poisson-Boltzmann equation (Jurrus et al., 2018) to determine the electrostatic potential generated by the nucleic acid on the sensing surface.

3. Result and discussion

3.1. Design of SpLig-HEMT biosensor

The AlGaN/GaN HEMT was fabricated using the methodology described in our previous study (Yang et al., 2024). As shown in Fig. 1a, the Au source, drain, and gate electrodes were deposited via vacuum evaporation. The patterned AlGaN/GaN channel was placed between the source and drain electrodes, and an insulating layer was placed on the left side for electrode encapsulation. Au was selected as the gate electrode because of its suitability for nucleic acid modification. As depicted in Fig. 1b, the clean Au electrode was functionalized with thiolated DNA anchor probes via Au-S bonding, followed by the blocking of unreacted Au sites with 6-mercapto-1-hexanol (MCH). Bovine serum albumin (BSA) was used to fill any remaining vacancies to reduce nonspecific binding. The presence of a specific miRNA analyte triggered a splint-ligation reaction that brought the reporter probe onto the gate surface (Fig. 1c). Both the reporter probe and miRNA molecule exhibit electronegative characteristics owing to their phosphate backbones, with the degree of charge varying according to the molecular length. In principle, our biosensor operates as an ion-sensitive field-effect transistor (ISFET) (Bergveld, 2003; Chu et al., 2017). When miRNA splint-ligation occurred on the surface of the Au gate electrode in this AlGaN/GaN HEMT biosensor, it generates an opposite charge in the HEMT channel, thereby modulating the channel conductance, resulting in a shift in the gate voltage (V_g). This regulates the channel current (I_{DS}), as expressed by Eq. (1):

$$I_{DS} = C_{OX}\mu\frac{W}{L}\left[\left(V_g - V_{TH}\right)V_{DS} - \frac{1}{2}V_{DS}^2\right] \quad (1)$$

where μ is the HEMT carrier mobility, W and L are the gate width and length, respectively, C_{ox} is the gate-to-channel capacitance, and V_{TH} and V_{DS} are the threshold voltage and drain-source voltage, respectively.

Thus, the sensing mechanism of the SpLig-HEMT biosensor is attributed to the potential variation at the gate electrode induced by the electronegativity of the reporter probe and miRNA. The magnitude of this potential shift, induced by target-driven splint ligation, is directly proportional to the concentration of the target miRNA.

3.2. Characteristics of SpLig-HEMT biosensor

In this study, we used miR-21 as a model to evaluate the developed biosensor for miRNA detection. We designed a pair of DNA probes targeting miR-21, including an anchor probe with a 5′ thiol modification and a reporter probe with a 5′ phosphorylated modification.

To confirm the successful modification of the DNA probe on the surface of the Au gate electrode, we measured the transfer and output characteristic curves of the HEMT biosensor. As shown in Fig. 2a, after DNA probe functionalization, the transfer characteristic curve displayed a significant right shift, and the output curve showed a corresponding decrease in current, indicating successful functionalization of the Au gate electrode surface. The morphology of the gate area before and after anchor-probe immobilization was characterized using atomic force

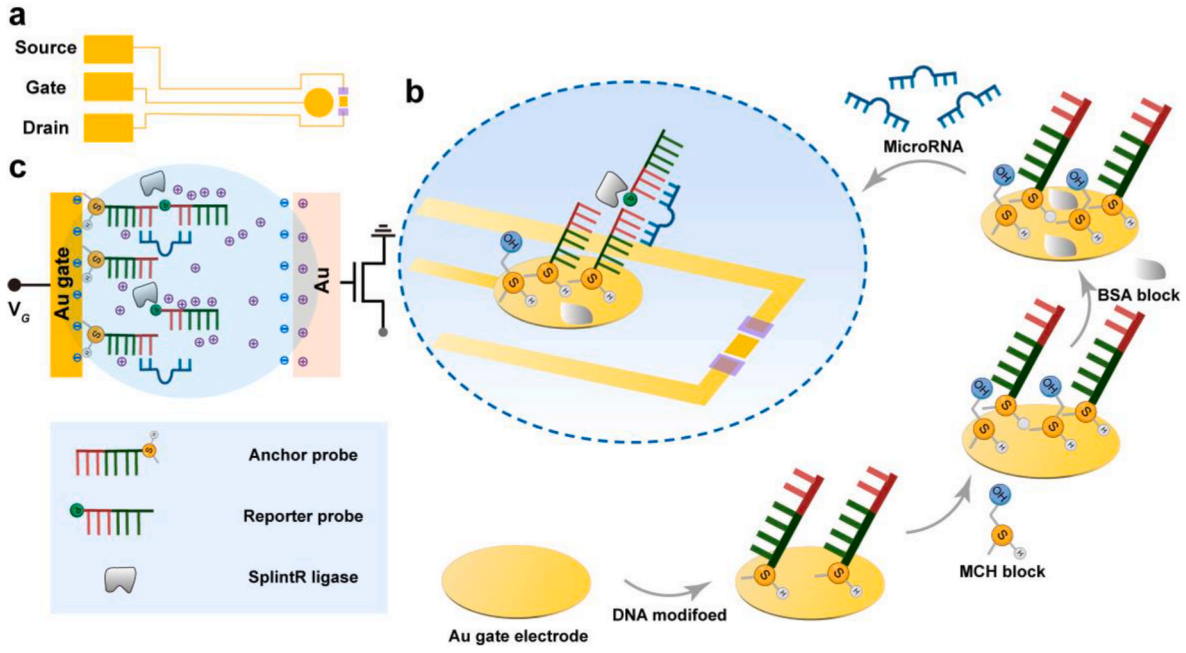

Fig. 1. Overview of the SpLig-HEMT Biosensor for miRNA detection (a) Schematic of the three electrodes configuration of HEMT. (b) Illustration of the construction and detection of SpLig-HEMT for miRNA. This process includes DNA modification, MCH and BSA blocking, and the splint-ligation reaction initiated by the target microRNA. (c) Illustration of surface charge alteration resulting from the splint-ligation product.

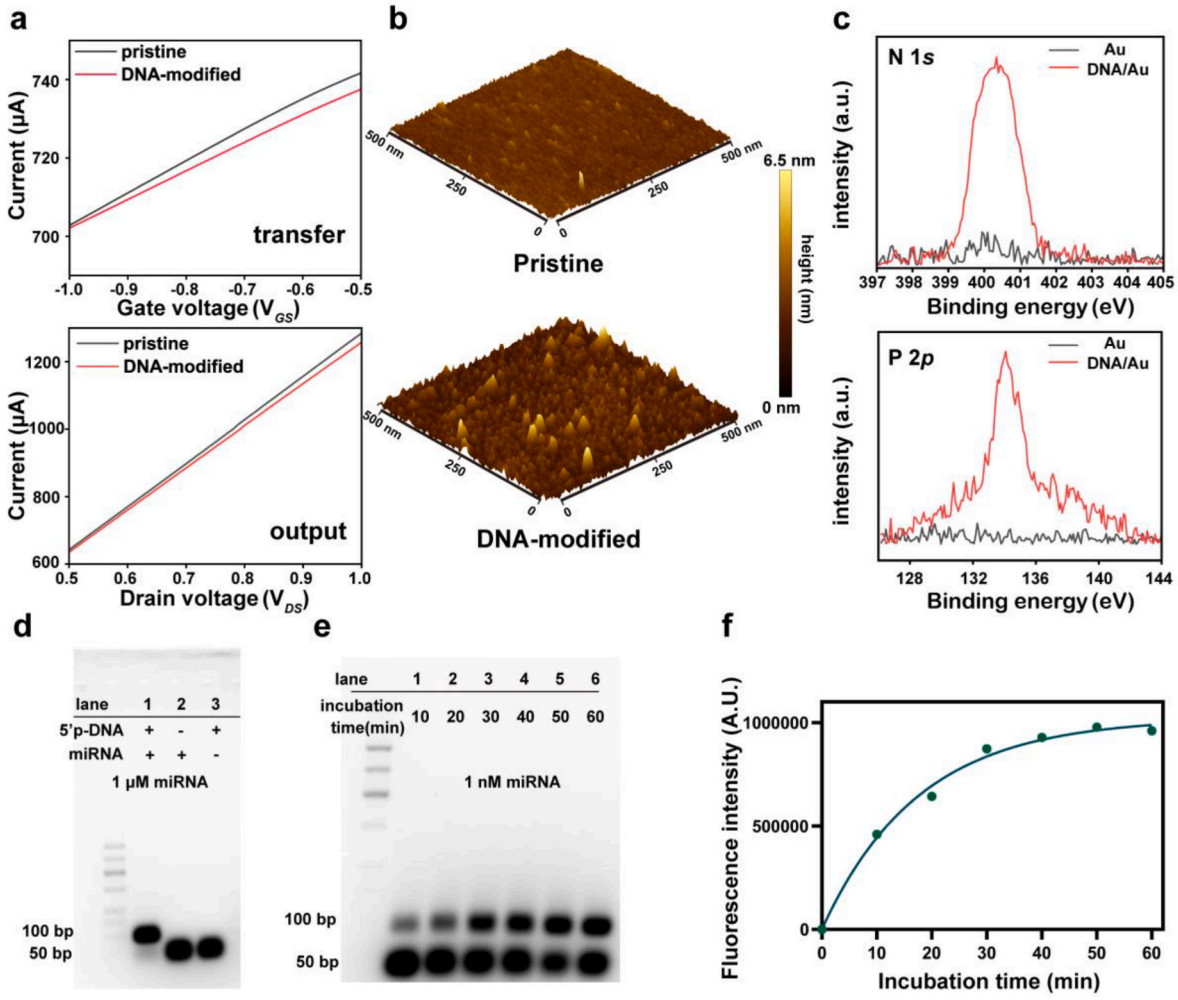

Fig. 2. Characterization of functionalized HEMT sensor. (a) Transfer characteristic curves and output characteristic curves of HEMT biosensor before and after biofunctionalization. (b) AFM image of Au gate electrode modified with DNA probe. The color bar indicates the height of the scanned surface. (c) XPS N_{1s} and P_{2p} spectroscopy of Au gate electrode before and after biofunctionalization. (d) Gel analysis of ligation products. Lanes 2 and 3, where either the reporter probe or 1 μM miRNA was absent, serve as a negative control. bp: base pair. (e) Effect of incubation time on ligation products. The ligation reaction was conducted at 25 °C with 1 nM miRNA and various incubation times. (f) Fluorescence intensity of the ligation product as a function of incubation time. (For interpretation of the references to color in this figure legend, the reader is referred to the Web version of this article.)

microscopy (AFM) in air. The pristine gate surface had a flat surface with a height of 0.5–1 nm, whereas the immobilized gate had a height of 4–4.5 nm, and the roughness value (Rq) for before and after functionalization are 0.490 nm and 0.852 nm, respectively (Fig. 2b). X-ray photoelectron spectroscopy (XPS) was performed to further evaluate the modification efficiency. After the DNA probe was modified on the sensing surface, N_{1s} and P_{2p} show great reinforcement appeared at 399.8 and 134.4 eV (Fig. 2c). These characterizations from the electrical tests, AFM, and XPS collectively confirm the successful immobilization of the anchor probes onto the sensing area.

3.3. Optimization of splint-ligation reaction

Splint-ligation was performed using SplintR ligase in the presence or absence of the target RNA and reporter probe. As shown in Fig. 2d, the reporter probe labeled with the correct ligation product (length: 110 bp) was successfully generated only when both the probes and target RNA were included in the ligation mixture. To optimize the SplintR ligase-mediated nucleic acid ligation reaction in the SpLig-HEMT system, we performed ligation reactions using a miRNA concentration of 10 pM and varied the reaction time from 10 to 60 min. As shown in Fig. 2e, a smeared band around the 100 bp region appeared after 10 min, indicating the initiation of ligation. The extension of the reaction time to 30 min resulted in a significant increase in ligation products. Although further incubation from 30 to 60 min continued to increase the product yield, the rate of increase was lower than the rapid growth observed within the first 30 min (Fig. 2f). To balance the detection time and sensitivity, we selected the 30-min reaction time for subsequent experiments.

3.4. Detection sensitivity of SpLig-HEMT biosensor for miR-21

To evaluate the detection performance of the SpLig-HEMT biosensor, we selected miR-21 as the target analyte because of its overexpression in various cancers and its potential as a biomarker for early diagnosis of cancer. In SpLig-HEMT, the specific recognition of miR-21 was achieved through SplintR ligase-mediated Splint-ligation (Fig. 3a). For comparison, we developed a ssDNA-HEMT biosensor that detected miR-21 via hybridization with a ssDNA probe (Fig. 3b).

In HEMT devices, the Debye length is crucial for the detection sensitivity because it defines the effective range within which electrical charges in a solution can influence the electric field at the gate surface. If the Debye length is shorter than the distance between the biomolecular charge (for example, miRNA or probe) and the gate surface, the change

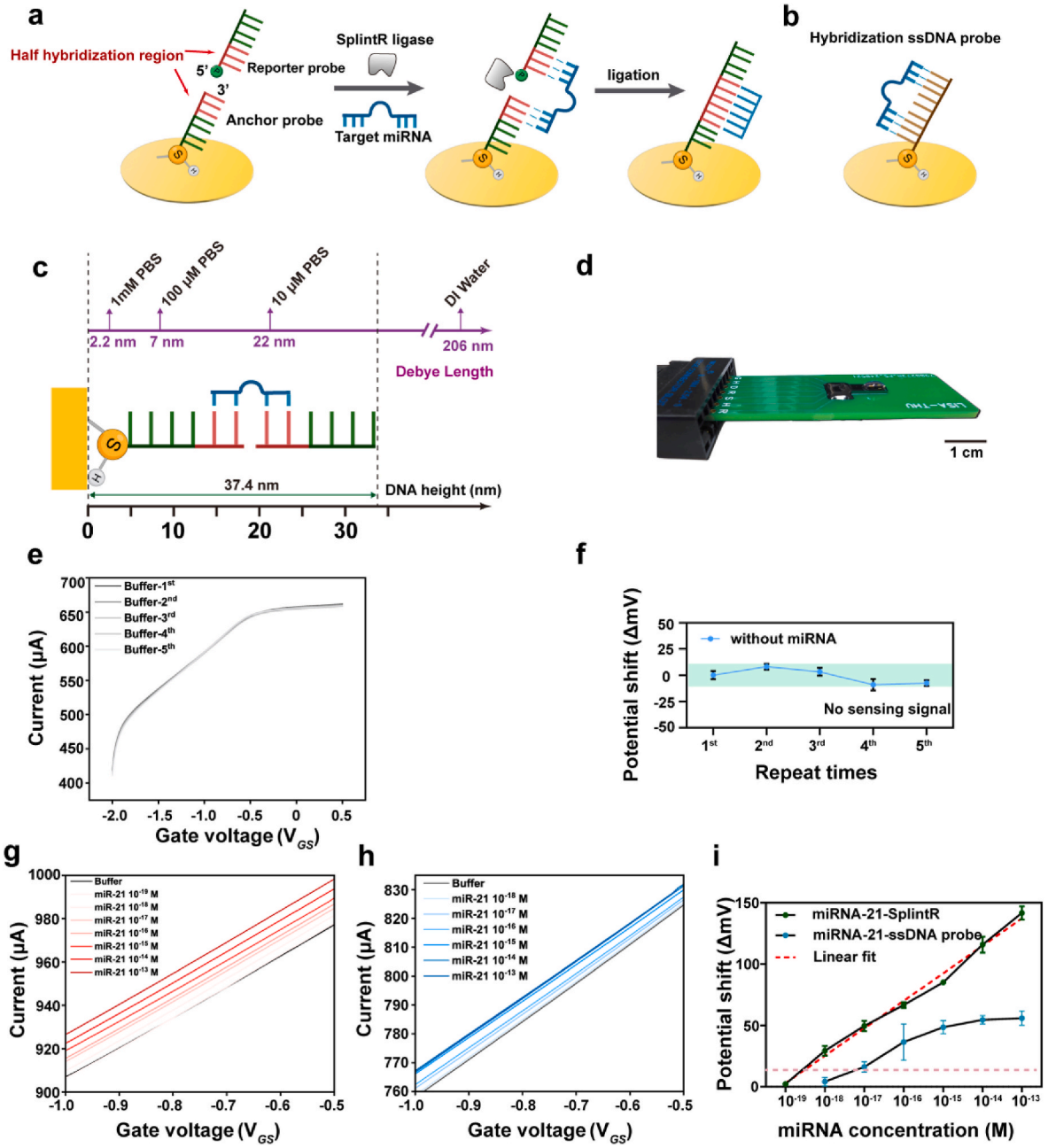

Fig. 3. Sensitivity of miRNA detection using SpLig-HEMT biosensor. (a) Schematic of splint-ligation on the sensing area of HEMT. This method depends on the ligation between the pre-modified anchor probe and reporter probe, with both of them hybridizing to adjacent sites of the target sequence. (b) Schematic of ssDNA-HEMT biosensor. This method depends on the hybridization of the ssDNA probe to the target miRNA. (c) Variation in the Debye length in PBS solution with the height of the ligation product. (d) Photograph of integrated HEMT chip. (e) Transfer characteristic curve of SpLig-HEMT measured after five consecutive additions of ligation mixture without target miRNA. (f) Potential shift as a function of repeat times with SpLig-HEMT biosensor. (g) Transfer characteristic curve of SpLig-HEMT biosensor measured after exposing miR-21 with increasing concentration from 10^{-19} M to 10^{-13} M. (h) Transfer characteristics curve of ssDNA-HEMT biosensor after exposing miR-21 with increasing concentration from 10^{-18} M to 10^{-13} M. (i) Potential shift as a function of miRNA-21 concentration in logarithm scale for SpLig-HEMT ($R^2 = 0.9872$) and ssDNA HEMT ($R^2 = 0.8768$) biosensors. The red dashed line represents the cutoff potential shift. Each data point represents the mean value ± standard deviation from three independent measurements. (For interpretation of the references to color in this figure legend, the reader is referred to the Web version of this article.)

in the charge-induced potential is significantly attenuated, leading to a reduced sensitivity of the HEMT device. The Debye length is closely related to the ion concentration of the electrolyte solution and is expressed as follows:

$$\lambda_D = \frac{1}{\sqrt{4\pi l_B \sum_i \rho_i z_i^2}} \quad (2)$$

where l_B is the Bjerrum length (0.7 nm), and ρ_i and z_i are the density and valence of the i-th ionic species, respectively. Fig. 3c shows the variation in Debye length at different concentrations of phosphate-buffered saline (PBS). In our detection system, the splint-ligation products were approximately 110 base pairs (bp) in length (Lohman et al., 2014), corresponding to an overall length of approximately 37.4 nm, as a single DNA strand extends to approximately 0.34 nm per nucleotide (Gür et al., 2021). To minimize the detection of charges beyond the Debye length,

we used deionized water as the reaction solution instead of PBS buffer.

The detection process was implemented on a portable integrated chip (Fig. 3d). Considering that the reaction volume on the sensing area was only 10 μL, we investigated whether frequent manual operations involving small volumes, such as rinsing and sample addition, could impact the stability of the SpLig-HEMT biosensor. We performed five consecutive sample additions without miRNA and observed negligible potential shifts (Fig. 3e). These results confirm that manual operation does not adversely affect biosensor performance (Fig. 3f). The cut-off value was determined to be three times the signal variation of the blank control (6 * 3 = 18 mV). Furthermore, to examine the feasibility of our HEMT biosensor for clinical testing, a long-term test was conducted after the devices were biofunctionalized with anchor probes. Fig. S2 displays the representative transfer curve obtained after varying days of storage, the value of V_{GS} remains nearly constant even when the SpLig-HEMT biosensor was immersed in a liquid environment for four days.

To further evaluate the detection range and sensitivity of our biosensor, the detection process was performed in two steps. First, varying concentrations of miRNA-21 were introduced into the ligation mixture and incubated on the sensing surface at room temperature. Subsequently, the device was rinsed three times with deionized water before conducting the measurements. The transfer characteristic curve exhibited a 141.6 mV potential shift as the miR-21 concentration increased from 10^{-19} M to 10^{-13} M (Fig. 3g), demonstrating a good concentration-dependent reaction. In comparison, the same bulk solution applied to the ssDNA-HEMT biosensors yielded a potential shift of 41 mV (an increase from 10^{-18} M to 10^{-13} M), as shown in Fig. 3h. The limit of detection (LOD) was calculated as three times the standard deviation of the control group. The LOD for the SpLig-HEMT and ssDNA-HEMT biosensors were estimated at 10^{-18} M and 10^{-17} M, respectively (Fig. 3i). At analyte concentrations below the LOD, the response signal becomes indistinguishable from noise. Moreover, the SpLig-HEMT biosensor demonstrated a good linear correlation (R^2 = 0.9872) between potential shift and miRNA-21 concentration (log scale) compared to the ssDNA-HEMT biosensor (R^2 = 0.8768). These results indicate that the Splint-Ligation reaction enhances detection sensitivity. We propose that this reaction introduces long-tailed reporter probes onto the sensor surface, which increases charge accumulation and amplifies the observed potential shifts. As shown in Fig. S3, the miRNA-21 molecule exhibits a net charge of −21 e, whereas the miR-21-reporter probe complex displays a net charge of −62 e.

In addition, HEMT device also contribute to the ultrasensitivity of our biosensor. First, the high-density, high-mobility two-dimensional electron gas underneath the HEMT sensing area provides excellent transconductance on the order of milli-Siemens, which significantly enhances the signal amplification capability. Second a uniform passivation layer (SiOx/SiO2) is deposited to suppress gate leakage, further improving the device performance.

3.5. Specificity of the SpLig-HEMT biosensor

To evaluate the specificity of our biosensor, we measured its response to a panel of miRNAs—miR-21, miR-144, miR-200c, miR-125 b, as well as a blank negative control (NC) (Fig. 4a). Upon addition of 10^{-14} M miR-21, a significant potential shift of 124.6 mV was observed, while the same concentration of the other miRNAs elicited only minimal potential shifts (Fig. 4b). Importantly, none of these interferents induced signal changes exceeding three times the response of the negative control, which were considered undetectable (Fig. S4).

To further validate the specificity of the SpLig-HEMT biosensor, we engineered a series of single-nucleotide mismatch variants of miR-21 and recorded their transfer characteristic curves over a concentration range from 10^{-18} M to 10^{-14} M. Given that the eight nucleotides at the 5' end of the mature miRNA, known as "seed region," are critical for

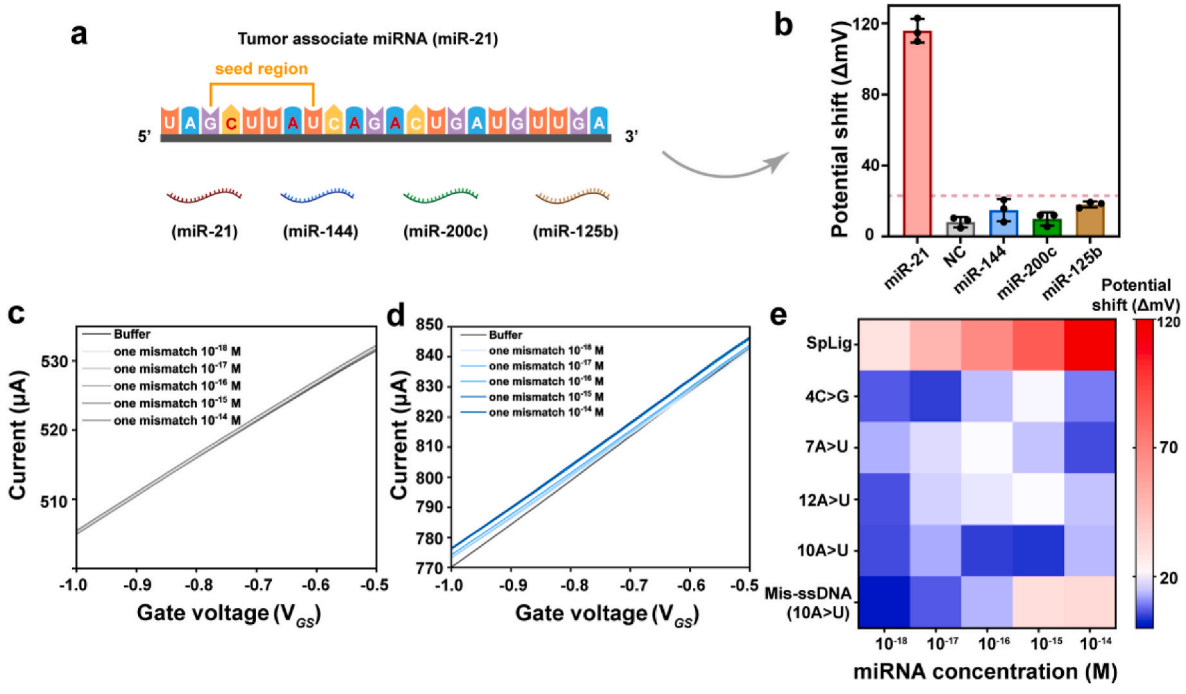

Fig. 4. Specificity of the SpLig-HEMT biosensor. (a) Schematic of miR-21 and different miRNA interferences. The nucleotide mutation site is marked with red. (b) Potential shift observed in the SpLig-HEMT biosensor on the addition of miR-21, miR-144, miR-200c, miR-125 b, and a noncomplementary sequence, each at a concentration of 10^{-14} M. (c) Transfer characteristic curve of SpLig-HEMT biosensor measured on the addition of single base mismatched (10 A > U) miR-21 at concentrations from 10^{-18} M to 10^{-14} M. (d) Transfer characteristic curve of ssDNA-HEMT biosensor measured on the addition of single base mismatched (10 A > U) miR-21 at concentrations from 10^{-18} M to 10^{-14} M. (e) Heat map showing the average potential shift values using SpLig-HEMT and ssDNA-HEMT biosensors to detect series of single-nucleotide mismatch sequence of miR-21 (4C > G, 7 A > U, 10 A > U, and 12 A > U) at concentrations of 10^{-18} M to 10^{-14} M, Signals under the cutoff value are presented in blue. The red dashed line indicates the cutoff potential shift. Each data point represents the mean ± standard deviation, obtained from three independent measurements. (For interpretation of the references to color in this figure legend, the reader is referred to the Web version of this article.)

physiological binding, we introduced mutations at two sites within the seed region (4C > G and 7 A > U) and two sites near the seed region (10 A > U and 12 A > U) to investigate the ability of the biosensor to distinguish between single-nucleotide mismatches (Fig. S5).

The SpLig-HEMT biosensor exhibited negligible signal shifts across this entire concentration range for these mismatches, whereas the ssDNA-HEMT biosensor displayed distinct potential shifts (Fig. 4c–d). Moreover, with successive additions of samples (10^{-18} M to 10^{-14} M), the SpLig-HEMT biosensor maintained a negligible signal shift for the four-point mutation (Fig. 4e). In contrast, the ssDNA-HEMT biosensor exhibited a significant potential shift in detecting the single-nucleotide mismatch miR-21 (10 A > U) at concentrations of 10^{-15} M (30 mV) and 10^{-14} M (34.3 mV), which exceed the 18 mV cutoff threshold. These findings demonstrate that the ssDNA probes lack the capability to specifically distinguish mismatched miRNA at concentrations above 10^{-15} M, underscoring the excellent specificity of our SpLig-HEMT biosensor in differentiating single-nucleotide mismatches.

This enhanced specificity stems from the SpLig-HEMT's dual probes recognition mechanism. The system requires perfect complementarity between the target miRNA and both the anchor and reporter probes to enable splint ligase-mediated ligation, effectively functioning as an AND-gate verification that minimizes false positives from mismatched sequences. Moreover, the ligase's faster turnover rate, lower apparent K_M, and higher proportion of direct ligation events compared with conventional T4 DNA ligases further contribute to the rapid and precise detection of target miRNAs.

3.6. Detection of miRNA in clinical serum samples

Ovarian cancer is a gynecological malignancy with the highest mortality rate, and its incidence is increasing globally (Siegel et al., 2024). Given that miR-21 is highly overexpressed in ovarian cancer serum and is recognized as a promising biomarker (Resnick et al., 2009), we evaluated the clinical applicability of the SpLig-HEMT biosensor for miR-21 detection. Clinical serum samples were obtained from ovarian cancer patients (samples S1–S10) and healthy individuals (samples H1–H10). Fig. 5a outlines the workflow employed for clinical sample analysis using the SpLig-HEMT biosensor.

Prior to analysis, serum samples were diluted in PBS at factors of 10^4, 10^5, 10^6, 10^7, and 10^8, and were directly assayed without any nucleic

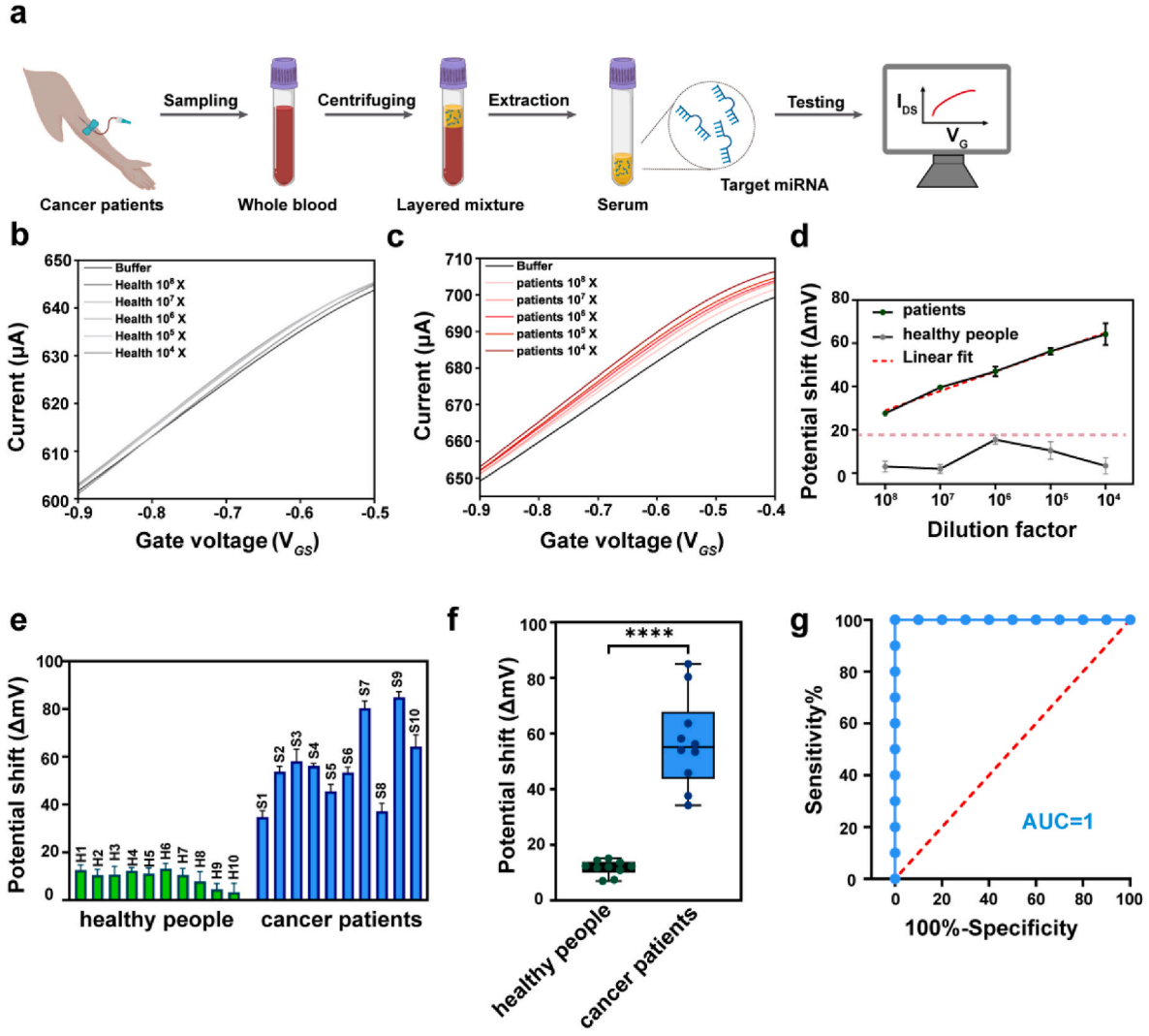

Fig. 5. Detection of miRNA-21 in clinical serum samples. (a) Workflow of miR-21 detection by SpLig-HEMT biosensor. (b) Transfer characteristic curve measured upon the addition of healthy individual serial sample H4 at dilution factor from 10^8-fold to 10^4-fold. (c) Measurement of serial serum samples from an ovarian cancer patient (S9) using the SpLig-HEMT biosensor. (d) Potential shifts versus serum dilution factors for ovarian patients and healthy individuals. The cutoff potential shift is highlighted by the red dashed line. (e) Potential shifts observed in diverse clinical serum samples. (f) Significant difference in miRNA-21 expressions levels between cancer patients and healthy individuals ($p < 0.0001$). (g) ROC curve analysis. Each data point represents the mean ± standard deviation, obtained from three independent measurements. (For interpretation of the references to color in this figure legend, the reader is referred to the Web version of this article.)

acid extraction or amplification. The successive measurements of healthy sample H5 across dilution factors (10^8 to 10^4) yielded minimal signal shifts, with potential changes ranging from 3.07 to 15.33 mV, all remaining below the cutoff threshold of 18 mV (Fig. 5b). In contrast, ovarian cancer sample S9 exhibited a potential shift of 27.57 mV even at a 10^8-fold dilution (Fig. 5c). Furthermore, a linear detection profile for miR-21 was established over the dilution range of 10^8 to 10^4 (Fig. 5d). We then measured 20 clinical samples and performed statistical analysis (Fig. 5e). Statistical analysis of 20 clinical samples demonstrated a significant difference in miR-21 expression levels between ovarian cancer patients and healthy controls ($p < 0.001$; Fig. 5f), confirming the biosensor's capability to discriminate between these groups. The receiver operating characteristic (ROC) curve further validated the diagnostic accuracy of the biosensor, with an area under the curve (AUC) of 1.0 (Fig. 5g), indicating excellent diagnostic accuracy. To further benchmark detection sensitivity, ELISA tests were performed to quantify human epididymis 4 (HE4) levels in clinical samples. HE4 was approved by the US Food and Drug Administration in 2011 as a diagnostic marker for ovarian cancer (Jacob et al., 2011). The ELISA results are consistent with our findings (Table S2). Importantly, the SpLig-HEMT biosensor requires only a minimal serum volume (1 μL), allowing for up to 1000 tests per 1 μL following dilution, and achieves results within 30 min. Providing a faster and more sample-efficient method than conventional ELISA.

4. Conclusion

In this work, we developed an SpLig-HEMT biosensor that integrates an RNA splint-ligation reaction with an AlGaN/GaN high-electron-mobility transistor for miRNA detection. The HEMT biosensor acts as a highly effective voltage amplifier to enhance detection sensitivity, whereas the splint-ligation reaction enables the precise discrimination of single-nucleotide mutations. The SpLig-HEMT biosensor achieves a detection limit of 10^{-18} M for miRNA-21, a widely recognized tumor biomarker, within only 30 min and with a dynamic range from 10^{-18} M to 10^{-13} M. This system shows no cross-reactivity with single-nucleotide-mismatched miRNA-21. Moreover, the SpLig-HEMT biosensor successfully facilitates direct analysis of blood serum samples, effectively distinguishing between healthy individuals and patients with ovarian cancer. This ability demonstrates its potential as a powerful diagnostic tool, addressing critical challenges in miRNA detection and expanding clinical applications in oncology. Moreover, the SpLig-HEMT demonstrate extensive versatility, enabling high-throughput, broad-spectrum identification of other miRNA, and selectivity through the design of anchor probes and reporter probes. In the future, integrating this biosensor into simple finger-prick devices can enable rapid and precise multi-biomarker detection in point-of-care testing. We believe that this work would be helpful for precise monitoring of cancer progression, metastasis, and recurrence, paving the way for more personalized treatment strategies and improved disease management across diverse conditions.

CRediT authorship contribution statement

Chenyang Yang: Writing – original draft, Writing – review & editing, Visualization, Investigation, Methodology, Conceptualization. **Jingya Tang:** Conceptualization, Methodology, Data curation, Visualization, Investigation. **Jianwen Sun:** Resources, Data curation, Visualization, Methodology. **Zewen Liu:** Methodology, Investigation. **Guoqi Zhang:** Methodology, Investigation. **Zhe Li:** Resources. **Dian-Bing Wang:** Methodology, Funding acquisition, Writing – review & editing, Writing – original draft, Investigation, Conceptualization. **Xian-En Zhang:** Investigation, Supervision, Writing – review & editing, Visualization, Methodology, Writing – original draft, Funding acquisition, Conceptualization.

Declaration of competing interest

The authors declare that they have no known competing financial interests or personal relationships that could have appeared to influence the work reported in this paper.

Acknowledgements

Special thanks to Jinyun Fang of the Technical Institute of Physics and Chemistry, Chinese Academy of Sciences for assisting with the AFM experiments. This work was supported by the National Key Research and Development Program of China (Grant No. 2022YFA1205804 and 2022YFC2303501), Major Project of Guangzhou National Laboratory (Grant No. GZNL 2024A01007), and the National Natural Science Foundation of China (Grant No. 32271489).

Appendix A. Supplementary data

Supplementary data to this article can be found online at https://doi.org/10.1016/j.bios.2025.117743.

Data availability

Data will be made available on request.

References

Balderston, S., Taulbee, J.J., Celaya, E., et al., 2021. Nat. Biomed. Eng. 5, 713–725. https://doi.org/10.1038/s41551-021-00706-z.
Bergveld, P., 2003. Sensor. Actuator. B Chem. 88, 1–20. https://doi.org/10.1016/S0925-4005(02)00301-5.
Bruch, R., Baaske, J., Chatelle, C., et al., 2019. Adv. Mater. 31, 1905311. https://doi.org/10.1002/adma.201905311.
Chen, C., Ridzon, D.A., Broomer, A.J., et al., 2005. Nucleic Acids Res. 33, 1–9. https://doi.org/10.1093/nar/gni178.
Chen, D., Huang, W., Zhang, Y., et al., 2023. Angew. Chem. Int. Ed. 62, e202304298. https://doi.org/10.1002/anie.202304298.
Choi, H.M.T., Chang, J.Y., Trinh, L.A., et al., 2010. Nat. Biotechnol. 28, 1208–1212. https://doi.org/10.1038/nbt.1692.
Chu, C.H., Sarangadharan, I., Regmi, A., et al., 2017. Sci. Rep. 7, 1–15. https://doi.org/10.1038/s41598-017-05426-6.
Gong, J., Tong, Y., Zhang, H.M., et al., 2012. Hum. Mutat. 33, 254–263. https://doi.org/10.1002/humu.21641.
Gür, F.N., Kempter, S., Schueder, F., Sikeler, et al., 2021. Adv. Mater. 33. https://doi.org/10.1002/adma.202101986.
Hughes, A.E., Bradley, D.T., Campbell, M., et al., 2011. Am. J. Hum. Genet. 89, 628–633. https://doi.org/10.1016/j.ajhg.2011.09.014.
Jacob, F., Meier, M., Caduff, R., et al., 2011. Gynecol. Oncol. 121, 487–491. https://doi.org/10.1016/j.ygyno.2011.02.022.
Jumper, J., Evans, R., Pritzel, A., et al., 2021. Nature 2021 596:7873 596, 583–589. https://doi.org/10.1038/s41586-021-03819-2.
Jurrus, E., Engel, D., Star, K., et al., 2018. Protein Sci. 27, 112–128. https://doi.org/10.1002/PRO.3280.
Klasens, B.I.F., Das, A.T., Berkhout, B., 1998. Nucleic Acids Res. 26, 1870–1876. https://doi.org/10.1093/nar/26.8.1870.
Li, B., Cao, Y., Sun, M., et al., 2021. FASEB (Fed. Am. Soc. Exp. Biol.) J. 35, e21916. https://doi.org/10.1096/fj.202100294RR.
Li, C., Li, Z., Jia, H., et al., 2011. Chem. Commun. 47, 2595–2597. https://doi.org/10.1039/c0cc03957h.
Lohman, G.J.S., Zhang, Y., Zhelkovsky, A.M., et al., 2014. Nucleic Acids Res. 42, 1831–1844. https://doi.org/10.1093/nar/gkt1032.
Matsuzaki, J., Ochiya, T., 2017. Int. J. Clin. Oncol. 22, 413–420. https://doi.org/10.1007/s10147-017-1104-3.
Nabhan, C., Raca, G., Lynn Wang, Y., 2015. JAMA Oncol. 1, 965–974. https://doi.org/10.1001/jamaoncol.2015.0779.
Navickas, R., Gal, D., Laucevičius, A., et al., 2016. Cardiovasc. Res. 111, 322–337. https://doi.org/10.1093/cvr/cvw174.
Phillips, E.A., Silverman, A.D., Joneja, A., et al., 2023. Nat. Biomed. Eng. 7, 1571–1582. https://doi.org/10.1038/s41551-023-01028-y.
Resnick, K.E., Alder, H., Hagan, J.P., et al., 2009. Gynecol. Oncol. 112, 55–59. https://doi.org/10.1016/j.ygyno.2008.08.036.
Richardson, K., Nettleton, J.A., Rotllan, N., et al., 2013. Am. J. Hum. Genet. 92, 5–14. https://doi.org/10.1016/j.ajhg.2012.10.020.
Sarangadharan, I., Regmi, A., Chen, Y.W., et al., 2018. Biosens. Bioelectron. 100, 282–289. https://doi.org/10.1016/j.bios.2017.09.018.
Siegel, R.L., Giaquinto, A.N., Jemal, A., 2024. Cancer statistics, 2024. CA Cancer J. Clin. 74, 12–49. https://doi.org/10.3322/caac.21820.

Varghese, A., Periasamy, C., Bhargava, L., 2018. IEEE Sens. J. 18, 9595–9603. https://doi.org/10.1109/JSEN.2018.2871718.
Wang, R., Wen, H., Xu, Y., et al., 2014. PLoS One 9. https://doi.org/10.1371/journal.pone.0113401.
Wang, R., Zhao, X., Chen, X., et al., 2020. Anal. Chem. 92, 2176–2185. https://doi.org/10.1021/acs.analchem.9b04814.
Woo, C.H., Jang, S., Shin, G., et al., 2020. Nat. Biomed. Eng. 4, 1168–1179. https://doi.org/10.1038/s41551-020-00617-5.
Yang, C., Sun, J., Zhang, Y., et al., 2024. Biosens. Bioelectron. 257, 116171. https://doi.org/10.1016/j.bios.2024.116171.
Yokoi, A., Matsuzaki, J., Yamamoto, Y., et al., 2018. Nat. Commun. 9, 2–6. https://doi.org/10.1038/s41467-018-06434-4.
Zheng, F., Chen, Z., Li, J., et al., 2022. Adv. Sci. 9, 2105231. https://doi.org/10.1002/advs.202105231.